ELSEVIER

Liquid crystalline reduced graphene oxide composite fibers as artificial muscles

Yuchong Gao, Jiaqi Liu, Shu Yang *

Department of Materials Science and Engineering, University of Pennsylvania, 3231 Walnut Street, Philadelphia, PA 19104, United States

Soft materials are known for their compliance, adaptivity and dexterity. They have been well-pursued to create artificial muscles for robotic applications, however, at the cost of load bearing, bit rates and energy efficiency compared with their rigid body counterparts. Despite significant efforts to improve their performance, very few can match the biological muscles, achieving fast speed, high elasticity, and high power density simultaneously. Here, we self-assemble composite fibers by wet-spinning graphene oxide (GO) nanosheets in their lyotropic liquid crystal (LLC) phase mixed with conducting polymers and depleting agent, poly(ethylene glycol), followed by chemical reduction of GO. The resulting reduced GO (rGO) nanosheets are highly aligned and closely packed, which is essential to their high mechanical strength and toughness and actuation behaviors. The composite fiber exhibits fast (80 ms) and reversible bending via electrostatic repulsion between the rGO sheets. When the fibers are plied with nylon yarns, our actuators can achieve 75 J/kg work capacity and 924 W/kg power density without diminishing the bending strain and efficiency up to 10,000 cycles.

Keywords: Artificial muscles; Graphene oxide; Fiber actuators; Lyotropic liquid crystals; Electrostatic actuation

Introduction

Biological skeletal muscles exhibit rapid (10 Hz), forceful (40 J/kg), and dexterous (35% strain) actuations [1], attributed to the unique hierarchical structures and functions [2] of the muscle fibers. Significant efforts have been made to create artificial muscles from soft materials or their hybrids [3,4] in response to external stimuli, including temperature [5], pressure [6], light [7], humidity [8], and electric field [9], surpassing biological muscles in one or few performance measures (Table S1) via meticulous material formulation and structural designs, at the cost of other performances. For example, through the reorientation of the aligned mesogens inside the polymer network during phase transition via electrothermal effect, liquid crystal elastomer (LCE) tubular actuators demonstrate large strains (35%) and work capacity (25 J/kg) with multimodal deformation[10]. Electrospun LCE fibers with diameter of 50 μm show fast actuation (16.7 Hz) and large power density (400 W/kg)[11]. However, the small diameters, intrinsic softness, and temperature-based actuation mechanism limit their mechanical strength, scalability, and efficiency to actuate large objects.

Compared to light, heat and humidity actuated fibers or artificial muscles, those stimulated by electric fields are generally faster and more forceful due to the more efficient energy distribution. They are also more compatible with the electrical control components and power supplies that are commonly used in established robotic manipulations. Paradox on actuation performance and the distinct limitations, however, still exist. For example, benefiting from the non-inversion symmetry of the crystal structures, electro-strictive actuators made from piezoelectric ceramics[12] can output over 100 MPa stress at a frequency of kHz at an actuation strain less than 2%. Electrochemically actuated artificial muscles[13–15] demonstrate tradeoffs between the actuator size, ion diffusion speed, and actuation strain. With

* Corresponding author.
E-mail address: Yang, S. (shuyang@seas.upenn.edu)

 https://doi.org/10.1016/j.mattod.2023.08.003

the rapid and strong Maxwell attraction force between the two flexible electrodes, dielectric elastomers (DEs) can achieve outstanding performance with up to 400% strain, ~5 MPa stress, larger than 100 Hz bandwidth, with an overall 20 J/kg work capacity and 600 W/kg power density[3]. However, ultrahigh voltage, requirement of pre-stretching[16] and multilayer structures[17] are often needed for large strains or high work capacity, which them vulnerable to electric breakdown and fabrication defects. Recently, through careful design of acrylate networks with short and long chains and dry stacking of them in multilayers, Shi et al. have achieved an impressive 88 J/kg work capacity and up to 670 W/kg power density[18]. Nevertheless, the DE stacks have relatively low stress output (0.4 MPa) and the performance quickly diminishes above 10 Hz due to the viscoelastic nature of the elastomers.

In contrast, rapid and forceful actuation through electrostatic repulsion between the stiff inorganic nanomaterials such as carbon nanotube (CNT) aerogel sheets has been reported[19]. The positively charged, closely aligned one-dimensional (1D) CNT forest bundles exhibit large expansion in width (220%) and high stress in length (3.2 MPa, 30 J/kg) at a speed on the order of millisecond under 5 kV input. The highly aligned CNT forests and their close approximation are the keys to realize appreciable electrostatic repulsion. However, it requires special fabrication tools and the actuation strain is limited in the aligned direction. Two-dimensional (2D) nanosheets, such as graphene[20], offer an ideal alternative. Macroscopic assemblies of graphene nanosheets can be achieved from the assembly of graphene oxide (GO)[21] dispersed in a polar solvent such as water[22], followed by reduction to form reduced GO (rGO). With the ultra-large surface area and outstanding charge storage capacity, rGO assemblies obtained from GO dispersion[23–25] have been exploited for applications such as supercapacitors[24] and solar cells[25].

Here, we exploit pre-assembly of GO sheets in their lyotropic liquid crystal (LLC) phase for high-performance electrostatic actuation. To enhance packing density for fast charge injection and high mechanical strength, we wet spin GOs in a fiber form together with the conductive polymer, poly(3,4-ethylenedioxy thiophene) polystyrene sulfonate (PEDOT: PSS), followed by chemical reduction of GO to reduced graphene oxide (rGO). Given the high conductivity, flexibility, ductility, water solubility[26], and strong affinity with GO sheets[27], PEDOT: PSS are chosen to mix with LLC GO, adding more elasticity to the brittle rGO fibers without hampering the charge injection performance. The morphology and ordering of the two components, the interaction and arrangement in the 1D fiber are carefully optimized during the wet-spinning process. The resulting rGO/PEDOT:PSS fiber shows outstanding mechanical properties (Young's modulus, toughness, and elongation-at-break) and exceptional electrical actuation performance. Further, the rGO/PEDOT: PSS fibers are plied with nylon yarns to enhance the actuation stability, demonstrating high work capacity (75 J/kg), actuation speed (16 Hz), power density (929 W/kg), and stress (2.62 MPa). We further demonstrate potential scalability of the fiber-based artificial muscles and their integration with robotic systems.

Results and discussions

GO dispersion (10 mg/mL, average lateral size ~ 1.3 ± 0.5 μm) and PEDOT: PSS solution are mixed at different mass ratios (2:8, 5:5, 8:2) and weight concentrations (11 mg/mL, 26 mg/mL, 52 g/mL) before being loaded into the syringe pump for wet spinning of GO/PEDOT: PSS fiber actuators (see Methods). The GO/PEDOT: PSS fiber is then stretched, chemical reduced, washed, and dried (Fig. 1**A, Fig. S1**). Stretching reduces buckling of the fiber upon drying as it will consume energy to straighten the fiber first before it is actuated. Precise control of the assembly structures of GO in the fiber is crucial to enable superior performance of the charge-injection-based electrostatic actuation. Oxide groups[28] on GO surface can prevent their aggregation, thus, enhancing the stability and ordering of GO sheets in an aqueous dispersion. When above a critical concentration, GO sheets align themselves along with a common director with a small interlayer spacing, forming the LLC phase with nematic ordering. This pre-ordering of the large, irregularly sized GO sheets into the nematic phase is essential for the GO dispersion to survive the initial contact with coagulation bath and be wet spun into free-standing fibers with closely packed GO. In our experiments, all the wet-spinning mixtures are concentrated to at least 40 mg/mL to form the LLC phase. As shown in Fig. 1B, the shear force induces the alignment of the LLC GO and PEDOT: PSS chains along the extrusion path, which is locked by the coagulation process where water is extracted, and the GO sheets are pushed closer to each other by the depletion force. Importantly, the addition of PEDOT: PSS should not disturb the LLC phase of GO dispersion, which is evaluated by polarized optical microscope (POM) (see **Fig. S2** and **Fig. S3**). We use an optimized combination of water extraction agent, acetic acid, long chain depletion agent, chitosan[29], and ionic crosslinker, calcium ions to obtain the zigzag closely packed morphology of the GO sheets (**Fig. S4**). Moreover, the weight ratio between GO and PEDOT: PSS is controlled at 8:2 (denoted as 8–2 GO/PEDOT: PSS) to obtain the brick-and-mortar like structures, with PEDOT: PSS located in-between GO sheets (**Fig. S5**). We note that low molecular weight polyethylene glycol (PEG) is added into the spinning mixture to serve as a deplete agent, which pushes GO sheets closer to each other. PEG also acts as a co-solvent for PEDOT and PSS[30]. Thus, it regulates the morphology of the polymer chains for increased toughness and elasticity of the fiber, without decreasing the electrical conductivity (**Fig. S6**). With the fine-tuned spinning mixture, coagulation bath, and spinning parameters, we can fabricate 8–2 GO/PEDOT: PSS fibers up to 10 m long.

GO is then chemically reduced to rGO by hydroiodic acid[31] to increase electrical conductivity, while preserving the close packing morphology without degrading the conductive polymers in the fiber (Fig. 1**C**) and their ability to increase the charge accumulation (i.e., capacitance) of the system[32]. High electrical conductivity (212 S/cm), high mechanical strength Young's modulus (~1 GPa), and a large strain-at-break (~16%) as seen in **Fig. S7** are achieved as a result of the closer rGO sheet-sheet distance and denser packing of the PEDOT and PSS chains,

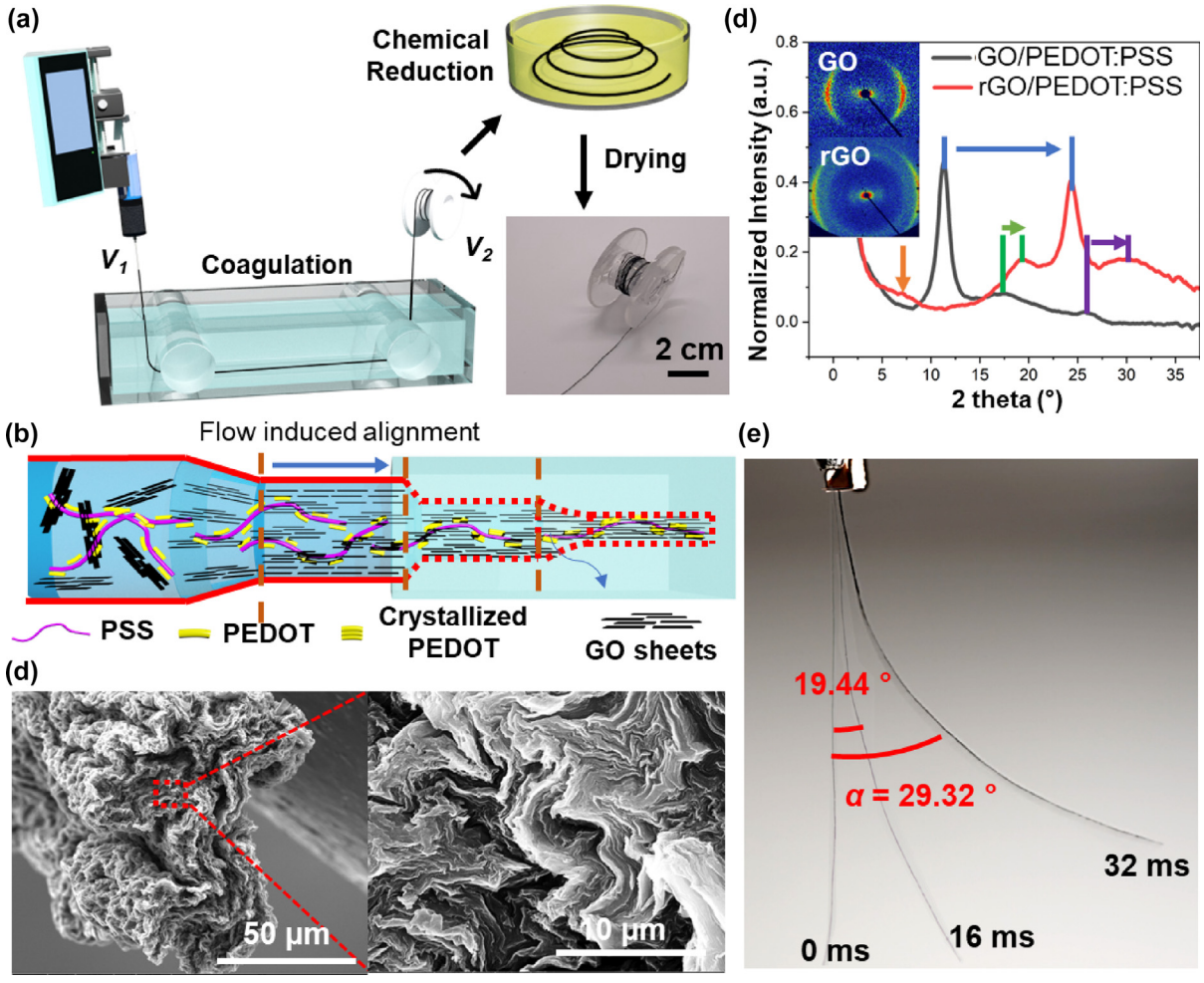

FIG. 1

Fabrication and characterization of rGO/PEDOT:PSS fiber actuators. (**A**) Schematic of the fabrication procedures, including wet-spinning and chemical reduction. Bottom right: photo of a dried two-meters long 8–2 rGO/PEDOT:PSS fiber winded on a spool. (**B**) Schematic depicting the alignment and packing of the GO sheets together with PEDOT:PSS polymer chains during the wet-spinning process. (**C**) Cross-sectional scanning electron microscopy (SEM) images of 8–2 rGO/PEDOT:PSS fiber at different magnification, showing the zig-zag close-packing morphology of the rGO sheets with PEDOT:PSS chains in-between. (**D**) Azimuthal integration of SAXS curves of 8–2 GO/PEDOT:PSS fiber (black) and 8–2 rGO/PEDOT:PSS fiber (red), showing decreased distance between rGO sheets (blue arrow), PEDOT (purple arrow), and PSS (green arrow) chains after reduction. Inset: 2D SAXS patterns of the fibers. (E) Photo of the 8–2 rGO/PEDOT:PSS fiber (50 μm in diameter, 55 mm in length) bent under 5 kV.

which is evident by the peak shift in the small-angle X-ray diffraction (SAXS) azimuthal integration curve (Fig. 1**D**), from 11.43° to 24.27°, corresponding to the layer spacing reduction from 7.71 Å to 3.66 Å. We note that the typical d-spacing in a wet-spun rGO fiber is 3.3 to 3.9 Å[33]. Assuming PEDOT: PSS chains co-exist with rGO in a brick-and-mortar manner, the d-spacing of 3.66 Å here indicates the high packing density of rGO sheets inside the fiber. Moreover, the peaks corresponding to 2θ of PEDOT (25.45°) and PSS (17.61°) have shifted towards higher angles, 30.30° and 19.83°, respectively. The decreased distance between the polymer chains further supports denser arrangement of rGO sheets. The emergence of the PEDOT crystal peak at 6.6° on the 8–2 rGO/PEDOT: PSS fiber curve further proves that the polymer chains inside the fiber are closely packed in an ordered morphology. The rGO fibers with optimized structure are denoted as 8–2 rGO/PEDOT: PSS fibers.

Fig. 1E shows the actuation behavior of the 8–2 rGO/PEDOT: PSS fiber (50 μm in diameter and 55 mm in length) under 5 kV applied voltage. The fiber actuator reaches a stable bending angle α of 29.32° in 32 ms. This response results from applying the positive voltage to the fiber with respect to a distant ground electrode, after which the injected positive charges make the closely packed rGO sheets carry the same sign of charges. The rapid electrostatic repulsion between the sheets triggers the increase of the layer spacing, while elastic restoration force provided by the stretched PEDOT: PSS guarantees the reversibility after the voltage is turned off (Fig. 2**A**). However, electrostatic repulsion behaviors are highly sensitive to the fabrication induced anisotropy as illustrated in Fig. 2**B**. A slight difference in packing density that occurs during the drying process can causes imbalanced force generation, influencing the macroscopic deformation response and its reproducibility. Winding the fiber

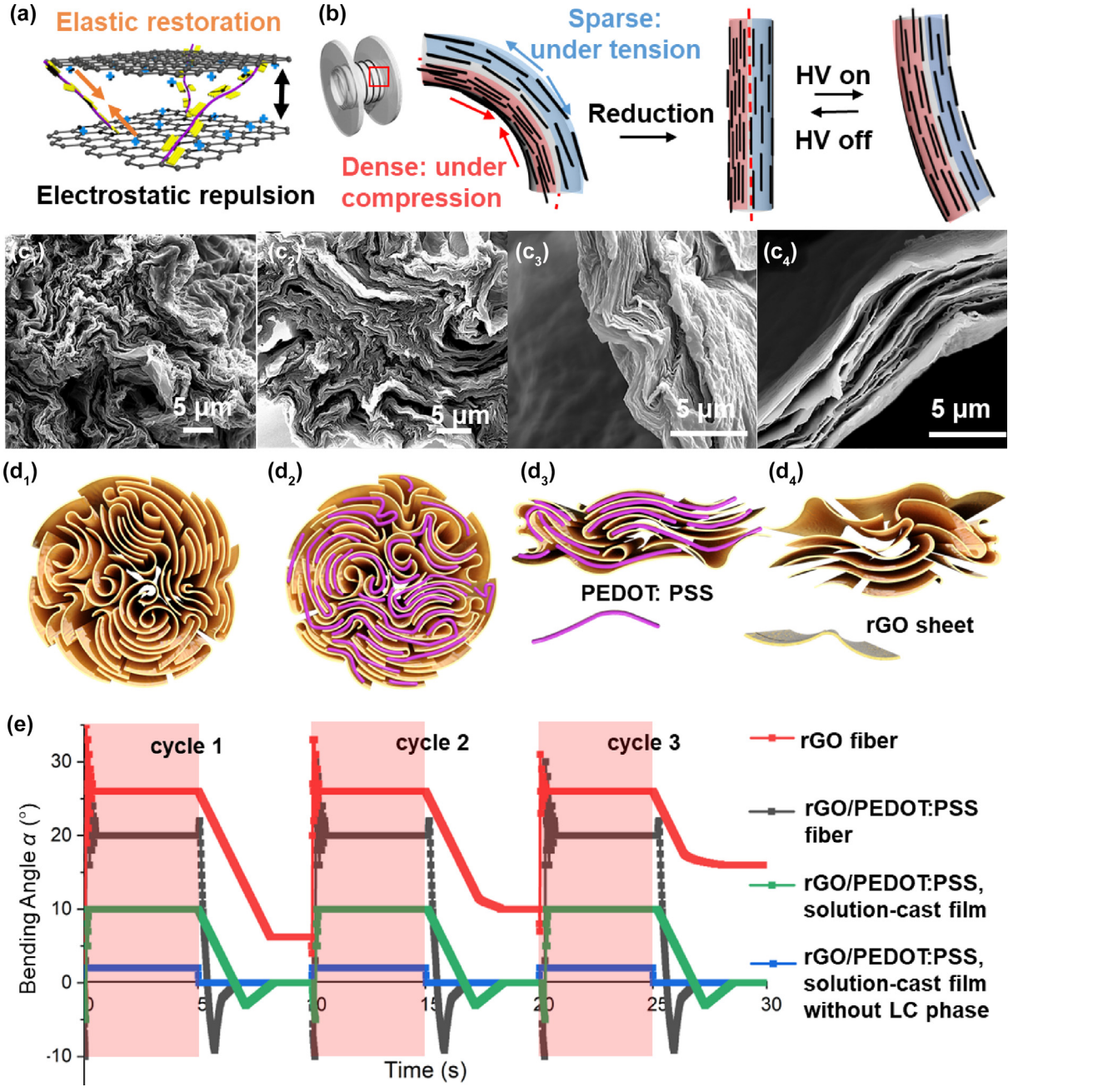

FIG. 2

Actuation performance of the single rGO/PEDOT:PSS fiber. (**A**) Schematic illustration of the electrostatic repulsion between rGO sheets.(**B**) Schematic illustration of the bending actuation mechanism under a high voltage (HV), as a result of anisotropic packing density induced during the spool collection after wet spinning. (**C**) Cross-sectional SEM images showing the packing and alignment of the rGO sheets and PEDOT:PSS chains in a rGO fiber without PEDOT:PSS (C_1), an 8–2 rGO/PEDOT:PSS fiber (C_2), an 8–2 rGO/PEDOT:PSS solution-cast film (C_3), and an 8–2 rGO/PEDOT:PSS solution-cast film without LC phase (C_4). (**D**) Schematic illustration of the packing and alignment of the rGO sheets and PEDOT: PSS chains in the four actuators observed in (C), depicting the absent of in-layer polymer chains in pure rGO fiber (D_1), zigzag brick-and-mortar close-packing of rGO/PEDOT: PSS fiber (D_2), less regulated lamellar brick-and-mortar structure in solution-cast rGO/PEDOT: PSS film (D_3), and large layer spacing in solution-cast rGO/PEDOT: PSS film without LC phase (D_4). (**E**) Bending angles of the four different actuators under 5 kV for extended time over 3 cycling tests.

on a spool during drying can induce compressive stress on the inner part of the fiber and tensile stress on the outer part. As water evaporates from the inner side of the fiber, an outer region with greater layer spacing between the rGO sheets (sparser) and an inner region with a smaller layer spacing (denser) is generated (Fig. 2B left). This gradient spacing is preserved throughout the rGO chemical reduction process since the elimination of the surface groups can only increase the uniformity of the packing (Fig. 2B middle). Hence, a straight fiber with gradient packing density along the radial direction will bend towards the sparse side (Fig. 2B right) as the electrostatic repulsion force F_D is a function of the layer spacing D[34] (see supplementary text and

Fig. S8 for more analytical analysis). To ensure the reproducibility of the packing anisotropy, hence the actuation performance, the diameter of the collecting spool is fixed at 50 mm for all the fibers fabricated in this work.

Accordingly, we systematically characterize the bending angle α of the fiber actuators of different lengths and diameters as a function of applied voltage (0.5–15 kV) as seen in **Fig. S9** and **Video S1**. α increases monotonically with the applied voltage in a certain range, which is correlated to the bending stiffness of the fiber. At the low applied voltage (less than 3 kV), α is negative, that is it bends towards the denser rGO packing side, and the magnitude of this negative bending increases with the compliance of the fiber actuators. We attribute this to the residual stress generated during fiber fabrication when it is stretched and dried after reduction. Load applied to straighten the initially buckled fiber can induce compression on the side with denser rGO packing and tension on the side with sparser rGOs, while the macroscopic shape is locked by strong sheet-sheet interactions during the liquid evaporation process before the load is removed. Therefore, as the rGO sheets repel each other and the sheet-sheet interaction drop sharply as D increases, the residual stress will bend the fiber in the opposite direction, towards the denser side, serving as a competing force as opposed to F_D. The range and magnitude of the negative bending are sensitive to manufacturing errors and predominated by the bending stiffness of the fiber. As soon as the difference in F_D caused by packing gradient (ΔF_D), which increases quadratically with the applied voltage, overcomes the residual stress, α starts to increase with increasing voltage. We note that there is no electrothermal effect at this high voltage since the current generated is negligible (**Fig. S10**). This observation not only proves that the actuation is solely caused by electrostatic generated force, but also indicates that there is no thermal annealing effect to release the residual stress. Therefore, upon turning off the voltage, the highly elastic rGO/PEDOT: PSS fiber will spring back to the straight form.

When the applied voltage is greater than 10 kV for a 50 μm-diameter and 55 mm-long fiber, oscillation caused by electromechanical instability dominates during actuation (**Fig. S11**). A negative damping effect is triggered at a high α when the deformation exceeds the critical value, beyond which the fiber tends to lower α to reach the equilibrium[35]. The high applied voltage, however, keeps F_D at a high magnitude and increase α again as soon as it is below the critical value (See supplementary text and Fig. S11 for details). No equilibrium state can be achieved, thus the fiber oscillates until the voltage is turned off. The onset voltage of the high-speed oscillation increases with the increase of the bending stiffness of the fiber. Specifically, the maximum voltage applied in this experiment (15 kV) is not enough to bend the 50 μm-diameter, 35- and 15 mm-long fibers to the critical α (observed at ~ 35° as shown in Fig. S9A), hence, it does not provoke oscillation in these fibers. Oscillation with positive damping at the beginning of the actuation and the overshooting immediately after the power is turned off (Fig. S9B) can be ascribed to the viscoelasticity of the polymer chains that lags behind the ultra-fast deformation of rGO sheets. Moreover, this delay from the polymer chains also slows down the recovery process driven by the elasticity provided by PEDOT: PSS.

Now we elucidate the importance of the zigzag close packing geometry in 8–2 rGO/PEDOT: PSS fiber (Fig. 2**C2**) to its actuation. For comparison, three other different actuators are fabricated, including the pure rGO fiber without PEDOT: PSS, and 8–2 rGO/PEDOT: PSS films with and without GO in the LLC phase. Pure rGO fiber does not benefit from the elasticity provided by the polymer chains for recovery (Fig. 2**C1**). 8–2 rGO/PEDOT: PSS film cast from the solution (52 mg/mL, same as the spinning mixture for 8–2 rGO/PEDOT: PSS fibers) has a less regulated packing morphology due to the lack of attraction and depletion force provided by chitosan and acetic acid in the coagulation bath and the physical confinement in the fiber (Fig. 2**C3**). In particular, the film cast from low concentration solution (13 mg/mL, no LLC GO phase) has much larger layer spacing where GO sheets are randomly dispersed in the solution and drop cast on the substrate (Fig. 2**C4**). Fig. 2**D** compares the structural differences in rGO sheets and PEDOT: PSS chains packing in the four actuators, whose morphologies are confirmed by the peak shift in SAXS curves displayed in **Fig. S12**. Correspondingly, large variations in mechanical properties are observed (**Fig. S13**). As opposed to 8–2 rGO/PEDOT: PSS fiber with high elasticity and toughness, rGO fiber itself is brittle and breaks at less than 4% of strain, the 8–2 rGO/PEDOT: PSS solution-casted film is weak (30 MPa tensile strength and 3% of strain) due to the lack of the close-packing morphology resulted from fiber coagulation process, while the film without LC phase is extremely fragile with 2 MPa tensile strength due to the large d-spacing hence weak sheet-sheet interactions. As exhibited in Fig. 2**E**, altering the optimized structure of 8–2 rGO/PEDOT: PSS fibers can dramatically impair the actuation performance. At a 5 kV applied voltage, 8–2 rGO/PEDOT: PSS fiber shows stable and reversible bending to 20°. In comparison, rGO fiber itself exhibits the largest deformation among four, up to 25°. However, due to the lack of elasticity provided by PEDOT: PSS, the fiber cannot be fully recovered to the original state (0°) and the degree of recovery is gradually reduced from cycle to cycle: the fiber stays at 7°, 11°, and 18° bending angles after 1, 2 and 3 cycles, respectively. The two film-based actuators have reversible deformation but at a much lower angle, 9.5° and ~ 2° with and without the LLC phase, respectively. Clearly, the synergistic effect of pre-ordering of GO sheets in the aqueous dispersion, fiber coagulation, and elasticity enhancement by PEDOT: PSS and PEG are essential to achieve the ultra-fast, reversible and repeated bending actuation.

Although the 8–2 rGO/PEDOT: PSS fiber can undergo 10,000 cycles at 5 kV without obvious decrease of the maximum bending angle, the maximum work capacity generated by a single fiber is no greater than 30 J/kg given by the small diameter (~50 μm) (**Fig. S14**). To realize more forceful actuation and increase the oscillation instability onset voltage, we ply rGO/PEDOT: PSS fibers with non-conductive nylon yarns together using a home-built plying machine (Fig. 3**A**). Nylon yarn is chosen because of its outstanding mechanical properties (~500 MPa tensile strength and up to 800 MPa Young's modulus), durability, low friction coefficient (~0.37) and low cost[36]. Five yarn actuators are fabricated, including r-r, r-n, r-n-r, n-r-n, and r-n-r-n where r refers to the rGO/PEDOT: PSS fiber and n refers to the

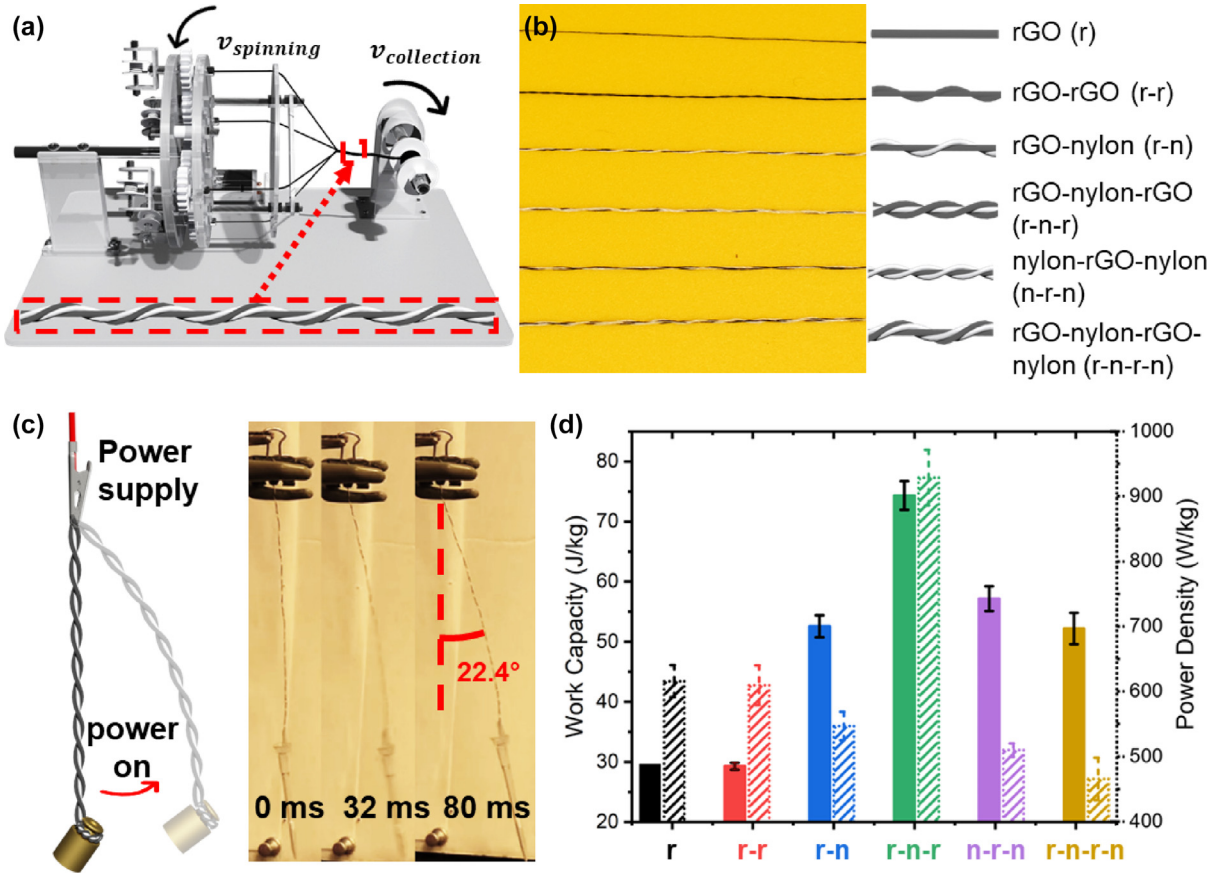

FIG. 3

Actuation performance of the plied rGO/PEDOT:PSS yarn actuators. (**A**) Schematic of the plying machine. (**B**) Photo (left) and schematics (right) of the six different fiber and yarn actuators, 8–2 rGO/PEDOT: PSS (r), two-ply rGO-rGO (r-r), two-ply rGO-nylon (r-n), three-ply rGO-nylon-rGO (r-n-r), three-ply nylon-rGO-nylon (n-r-n), and four-ply rGO-nylon-rGO-nylon (r-n-r-n). (**C**) Schematic (left) and photo (right) of a 1.1 mg r-n-r yarn lifting a 2-g weight in 80 ms with a bending angle of 22.4°, demonstrating a work capacity of 73.94 J/kg. (**D**) Chart of the maximum work capacity and power density of the six different fiber and yarn actuators, the actuation speed from left to right is 48 ms, 48 ms, 96 ms, 80 ms, 128 ms, and 112 ms, respectively. All results are averaged over 5 different yarn actuators fabricated with the same method.

nylon yarn (Fig. 3**B**). By balancing the requirement of large actuation strain, high instability onset voltage, and high mechanical strength, 8–2 rGO/PEDOT: PSS fibers with 50 μm diameters are chosen as they have the highest degree of alignment (**Fig. S15**). The bending actuation is preserved in the yarn actuators because the single rGO/PEDOT:PSS fibers rotate around the center axis in the plying process without self-entanglement, the relative positions of the dense and sparsely packed rGOs in a single fiber remain unchanged (**Fig. S16**), while the friction between individual fibers help to eliminate oscillation instability, providing extra damping (see explanation in supplementary text). Therefore, all the yarn actuators show stable bending actuation below 15 kV (**Fig. S17**). For the r-n-r yarn, two 8–2 rGO/PEDOT: PSS fibers bend towards the same direction and are stabilized by one nylon yarn in the middle. The electrostatically generated bending from two fibers constructively summed up without triggering electromechanical instability, exhibiting a maximum $\alpha \sim 50°$ at 15 kV. For other piled yarn actuators, however, the actuation speed and maximum α are limited due to the energy dissipation via friction between the fiber and the nylon yarn, and the increased bending stiffness of the plied yarns, respectively.

The improved force generated by the plied yarn actuators can be manifested in the weightlifting experiment as illustrated in Fig. 3**C** and **Video S2**. With a 2-gm weight (1,400 times heavier than the plied yarn itself) hung below the plied r-n-r yarn actuator, the yarn bends to 22.4° in ~ 80 ms at 5 kV applied voltage, realizing an average work capacity of 74.94 J/kg and a power density of 929 W/kg over 10 cycles, exceeding the typical performance of mammalian skeletal muscles[2]. Working against a load is more efficient than bending a free end actuator, because the tensile stress provided by the load can effectively decrease the energy loss during the initial oscillation by decreasing the amplitude of the swinging (**Fig. S18A**). Moreover, the gravity of the load can speed up the recovery process by assisting the elasticity of the polymer chains in the identical direction. The weightlifting experiments of rGO/PEDOT:PSS fiber and 5 different yarn actuators suggest that the plied yarn actuators generally have larger work capacity (**Fig. S18B-C** and Fig. 3**D**). The fiber and yarns have minimal relaxation and are highly stable due to

the majority composition of inorganic materials, maintaining the same bending angles up to 10,000 cycles at 10 kV without load (**Fig. S18D**). No heat is generated in the plied yarns during actuation (**Fig. S19**). The actuation speed, however, is diminished when incorporating non-conductive nylon yarns. It is worth mentioning that the absolute force output can be enhanced by plying more 8–2 rGO/PEDOT: PSS fibers and nylon yarns. As seen in **Fig. S20**, a 16-ply yarn can lift a 26g load up to 10.73° bending angle. The work capacity, however, is dropped to 12.38 J/kg due to frictions between the 16 individual fibers.

To compare the actuation performance of our actuators with other artificial muscles reported in literature, we construct an Ashby plot shown in Fig. 4 [2,3,6,7,9,11,18,36–40], including the work capacity and actuation bandwidth reported in literature (see Table S2). In general, speeding up the actuation will lead to significant decrease in either strain or stress, and vice versa. Here, our artificial muscle is capable of both the fast electrostatic actuation and high work capacity by taking advantage of the rapid charge injection process. The response speed of our actuators is determined by the conductivity and charge transportation pathway, while the work output during this process is governed by the amount of the charge injected and the distance between the repelling units. Therefore, we expect the structural optimization of rGO sheets and PEDOT: PSS chains can further increase the speed and work capacity collectively. Specifically, the large surface area of rGO sheets will increase the charges that can be injected, while packing GO closely and aligned along the fiber length with PEDOT: PSS in-between can enable fast transportation and large force output. Although increasing the work output by plying the fibers into yarns diminishes the bandwidth due to the energy consumed by friction, the rGO/PEDOT: PSS artificial yarn muscles still outperform biological muscles in both axes. Further we calculate the stress, strain, and actuation efficiency indirectly from the weightlifting experiments. We show that r-n-r yarn actuator exhibit larger stress (2.62 MPa), comparable strain and slightly smaller efficiency in comparison with those of the biological muscles [1,2] (**Fig. S21**). We attribute the superior performance to the LLC ordering of GO sheets pre-coagulation, high electrical conductivity of rGO, and high elasticity of PEDOT: PSS and PEG.

Next, we exploit the potentials of rGO/PEDOT: PSS yarn-based artificial muscles by constructing an insect wing-like structure. We thread four r-n-r yarns through the pre-designed holes and attach them to the wing-like skeleton cut from polyethylene terephthalate (PET) sheets (Fig. 5**A** and **Fig. S22**). The yarns bend and flap the whole wing downwards in 80 ms with 5 kV applied. We note that due to the bending elasticity of the PET skeleton, which offers boundary confinement of the yarns, at a higher flapping speed, the recovery of the wing tends to overshoot to an angle that is slightly negative after the voltage is turned off. As displayed in Fig. 5**B** and **Video S3**, the magnitude of the insect wing flapping motion (angle between the original position and the maximum deformation position of the wing) can be maintained at ~ 30° flapping angle when 5 kV is applied

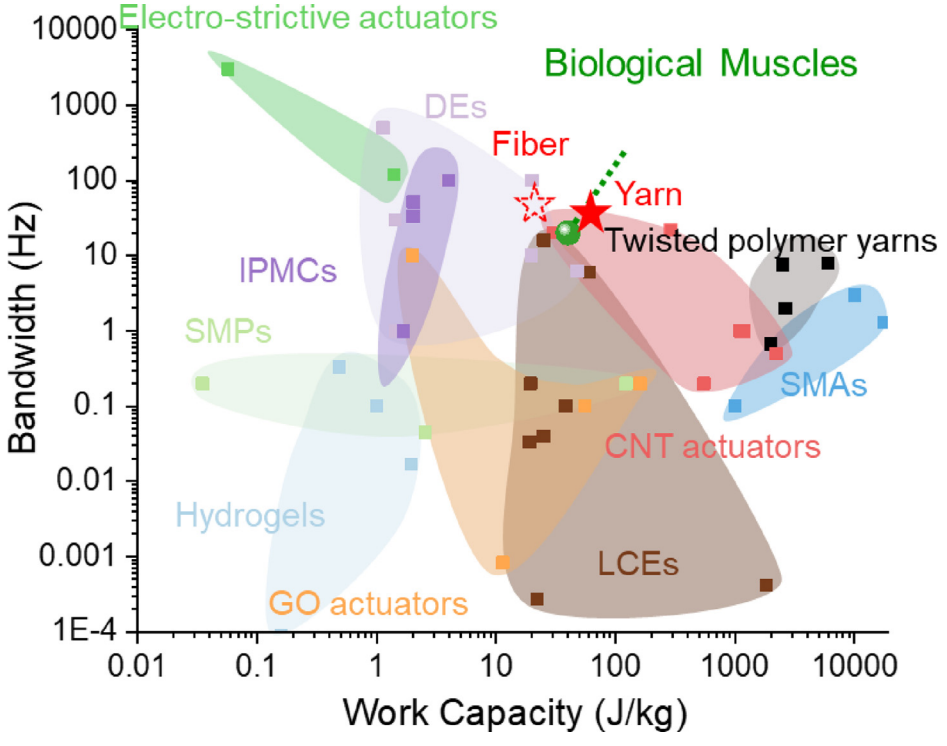

FIG. 4

Comparison between the rGO/PEDOT: PSS yarn actuators, biological muscles, and other artificial muscles reported in literature. Ashby plot comparing fiber and yarn actuators from this work, biological muscle[2], and state-of-the-art artificial muscles including electro-strictive actuators[3], shape memory alloys[6], LCEs[7,9],GO actuators[11], DEs[19], CNT fibers actuators[37], hydrogels[38], IPMCs[39], twisted polymer yarns[40], and shape memory polymers[41], in terms of bandwidth and work capacity.

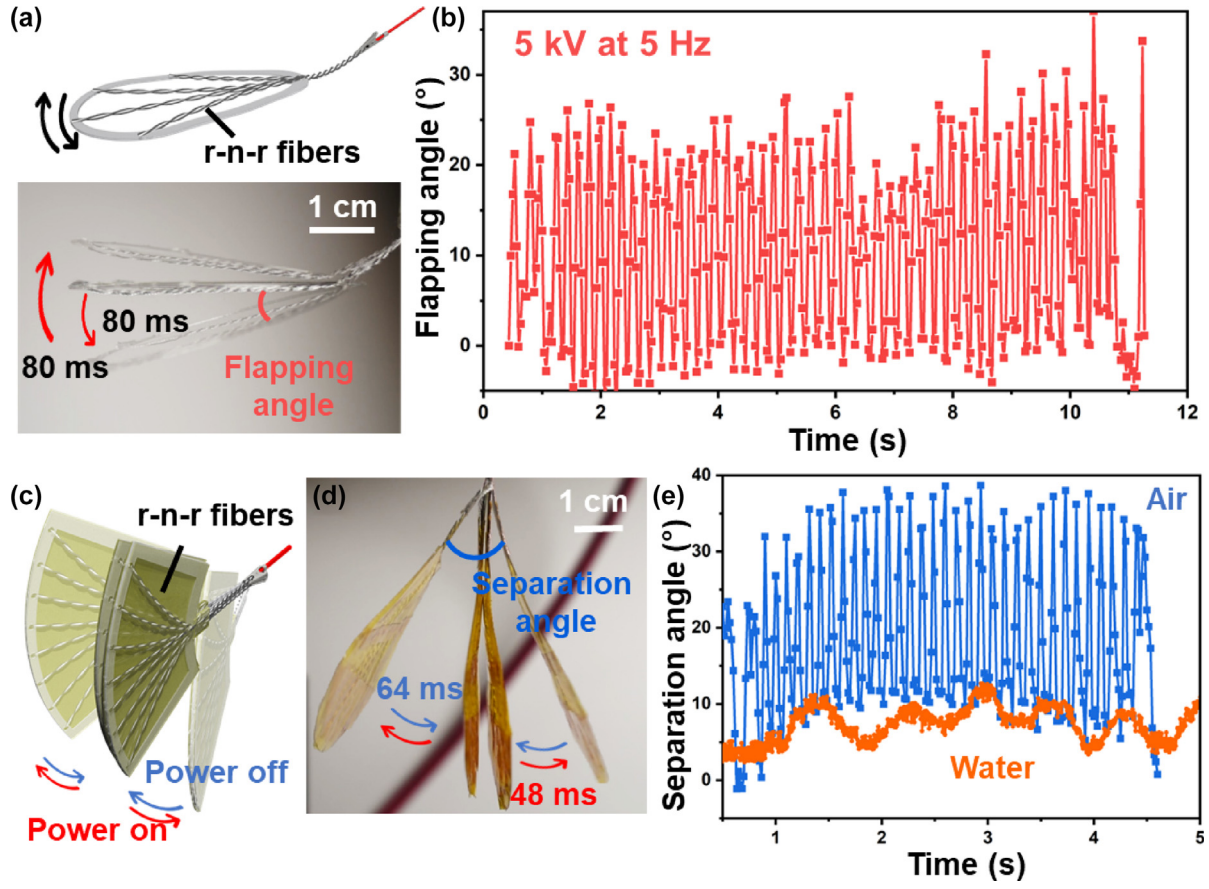

FIG. 5

Robotic demonstrations of the plied rGO/PEDOT:PSS yarn actuators. (**A**) Top: Schematic of a wing structure with a PET skeleton and threaded with r-n-r yarns for actuation. Bottom: photo of the wing structure flapping at ~5 Hz. (**B**) Flapping angle vs. time of the wing structure actuated under 5 kV at 5 Hz. (**C**) Schematic illustration of a fishtail actuator, consisting of two fish tail fins with a PET skeleton and threaded with r-n-r fibers for actuation. Kapton tape is applied to the fin for insulation. (**D**) Photo of the fishtail fins actuating at ~10 Hz. (**E**) Separation angle vs. time of the fishtail fins actuated in air and in water, respectively.

at a frequency of 5 Hz. Higher frequency motion can be achieved at the cost of flapping angle, for example, lowered to ~4° at 5 kV and 40 Hz frequency (**Fig. S23**). This is due to the hysteresis from the soft PEDOT: PSS chains, the amount of strain that can be recovered within the 12.5 ms interval between two cycles limits the achievable flapping angle at high frequencies.

The rapid electrostatic actuation gives us confidence to explore the feasibility of underwater devices. Previously, rapid heat dissipation in water would be detrimental to their performance in heat activated liquid crystal elastomer[7] and liquid metal[41] based soft robots. Here, two fishtail-like fin skeletons are cut from PET sheets and eight r-n-r yarn actuators are threaded through and attached to each fin. Kapton tape is then used as an insulation layer outside the entire fin to eliminate any possible electric leakage (Fig. 5**C**). Compared to a single flapping wing, two fins located next to each other response more rapidly in air when actuated jointly as shown in Fig. 5**D** and **Video S4**; the time needed to open the two fins is decreased to 48 ms. We attribute this mainly due to the macroscopic electrostatic repulsion between the two fins. Moreover, the slightly improved recovery speed in the fishtail device can be attributed to the assistance from the gravity. As a result, the separation angle between the two fins can be retained at 30° at 10 Hz in air, twice as fast as the flapping wing (Fig. 5**E**). However, in water, the fins experience much larger dragging force, thus their separation angle is reduced to ~10° at a frequency of 1.5 Hz. We believe these numbers could be improved with a better design of the wings and fins such as shown from the soft robotic dragonfly with flippy wings [42] and their miniaturization. The larger amplitude and faster speed was obtained from the dragonfly at the insect-scale (millimeter sized and light-weight, 317 mg), whereas our wing is ~2.5 cm × 5 cm, and the fin is 5 cm x10 cm; both have thickness ~0.5 mm.

Conclusion

We pre-order GOs in LLC phase, which is critical to their formation of zigzag brick-and-mortar close-packing of rGO in a fiber format, leading to superior actuation performance. Although dielectric elastomers and their composites have demonstrated high speed and high load bearing capacity in actuation, inorganic materials are typically introduced as minor additives and

their ordered assemblies in polymer matrix are not possible. In contrast, our system is mainly made of GOs and we address their brittleness by introducing PEDOT:PSS and PEG while enhancing the conductivity. In turn, it allows us to ply the fibers with conventional yarns, demonstrating work capacity and power density superior to biological muscles. In the future, we can take advantage of textile engineering techniques such as knitting and weaving to program the actuation behaviors while further improving the actuation strain and efficiency. Conceivably, the activation voltage can be lowered (and thus, increasing actuation efficiency) by increasing the conductivity of rGO/PEDOT: PSS and/or rGO to store more charges through approaches such as, assemblies of higher ordered GOs of more uniformed sizes, increasing crystallinity of rGOs[42], synergistic defect engineering of rGOs [43], fine-tuning of the chain length of PEDOT: PSS and GO reduction chemistry, and minimizing frictions between fibers and yarns.

Material and methods

Materials

Single layer graphene oxide (GO) aqueous dispersion (10 mg/mL, lateral size 0.5–2.0 μm) was purchased from ACS Materials. Poly (3,4-ethylenedioxythiophene)-poly(styrenesulfonate) (PEDOT: PSS) aqueous solution (1.1 wt%, Oragacon ICP-1050), polyethylene glycol 600 (PEG-600) and ethylene glycol (EG) (anhydrous, 99.8%), chitosan (high molecular weight, 310 k-375 k Da), calcium acetate (USP reference standard), calcium chloride (anhydrous, powder), hydroiodic acid (HI) (57%, for analysis EMSURE®), sodium bicarbonate (ACS reagent greater than 99.7%), and methanol (anhydrous, 99.8 %) were purchased from Sigma-Aldrich. Acetic acid (glacial, 99+%, Thermo Scientific™), ethanol (200 Proof, Decon Laboratories) were purchased from Fisher Scientific. Selric heavy duty nylon threads (white #69 T70, 210D/3, diameter 0.2921 mm) was purchased from Amazon.com.

Fabrication of the spinning mixture

The spinning mixture was prepared by mixing 10 mg/mL GO dispersion with PEDOT: PSS aqueous solution at a certain weight ratio (2:8, 5:5, and 8:2) in a glass vial using vortex mixer (Fisher Scientific Heavy-Duty Microplate Vortex Mixer) with addition of 10 wt% PEG-600. The total volume of the mixture was 4 mL, which was then concentrated to 1 mL by evaporating water over 2 h in an oil bath (60 °C) placed on a hotplate (IKA C-MAG HS 7). The concentrated mixture was vortexed for 8 h at a speed of 1000 rpm to ensure the homogeneity before loaded into the syringe for wet spinning.

Formulation of the coagulation bath

Two different optimized coagulation baths were used in this work. For spinning mixtures with GO/PEDOT: PSS = 8:2 wt/wt, a bath of 70 wt% acetic acid solution was made by mixing glacial acetic acid and DI water, and 1 wt% chitosan was added as depletion agent in 5 aliquots, each containing 0.2 wt% chitosan. The solution was magnetically stirred at 50 °C until it was homogenous before addition of the next aliquot. Then 5 wt% aqueous solution of calcium acetate was added into the solution in 5 aliquots as the ionic crosslinker of GO sheets, each aliquot contained 1 wt% aqueous solution of calcium acetate. The solution was magnetically stirred at room temperature until it was homogenous to add the next aliquot. The coagulation bath was cooled to room temperature before use.

For spinning mixtures with more PEDOT: PSS (e.g. GO/PEDOT: PSS = 2:8), the coagulation bath was made by mixing ethanol and DI water at a 3:1 v/v, followed by dissolving 3 wt % aqueous solution of calcium chloride into the mixture under sonication.

Wet spinning of GO/PEDOT: PSS fibers

The spinning mixture was loaded into a 1 mL syringe (Henke-Ject) and extruded through a blunt-tip needle (Gauge 18, 20, or 22) into the 3D printed coagulation bath (Fig. S1). The speed of extrusion was controlled by a syringe pump (Harvard Apparatus 11 Elite) at a constant, 55 μL/min. The as-spun GO/PEDOT: PSS fiber was carefully guided under the two horizontally placed rods to the rotating spool outside the coagulation bath for continuous collection. The speed of the rotating spool was set to a higher value to induce stretching on the fiber for better alignment of the GO sheets, the value was decided by the stretching ratio, which can be calculated from the linear speed of the extrusion and the linear speed of the collection,

$$Stretchingratio = \frac{v_{collcetion}}{v_{extrusion}} = \frac{\omega_{rpm} * 2\pi r_{spool}}{v_{ext}/\pi r^2_{sryinge}} \quad (1)$$

where ω_{rpm} is the angular rotation speed of the spool, r_{spool} is the radius of the spool, v_{ext} is the extrusion speed from the syringe, in the unit of μL/min, and $r_{sryinge}$ is the radius of the syringe. The stretching ratio of 1.44 was used throughout this work, which was the maximum without breaking the fiber. v_{rpm} was varied accordingly, with known spool and needle size, and extrusion speed. After collection, the GO/PEDOT: PSS fiber was air dried on the spool before reduction.

Study of ethylene glycol and PEG-600 treatment

GO/PEDOT: PSS fibers without PEG were fabricated following the same solution preparation and wet spinning process as described above. The ethylene glycol treatment of GO/PEDOT: PSS fibers was done by immersing the dried GO/PEDOT: PSS fiber into ethylene glycol in a closed container for 5 min, then collected on the spool and air dried. A swelling in diameter and straighten in length were observed after ethylene glycol treatment (Fig. S6).

Chemical reduction of rGO/PEDOT: PSS fibers

The dried GO/PEDOT: PSS fibers were immersed in hydroiodic acid in a glass vial and placed on a 65 °C hotplate for 24 h to get the maximized conductivity. After 24 h, the reduction container was cooled down to room temperature, the fibers were taken out and washed by saturated sodium bicarbonate aqueous solution, water, and methanol sequentially, to remove any excess residual chemicals. Finally, the rGO/PEDOT: PSS fibers were winded and fixed on a spool to air dry before any further testing.

Fabrication of rGO fibers without PEDOT: PSS

The neat rGO fibers were fabricated following the same steps as that for 8–2 rGO/PEDOT: PSS fibers. 10 mg/mL aqueous GO

dispersion was concentrated to 40 mg/mL by evaporating water in a 60 °C oil bath, followed by 8 h vortex homogenization. The high concentration GO dispersion was then loaded into a syringe with a blunt-tip needle, extruded into the coagulation bath at a constant speed of 55 μL/min, collected and dried on a spool after the water extraction process ends. The optimized coagulation bath for neat GO fibers was pure glacial acetic acid. After fully dried, the GO fibers were immersed in a hot (65 °C) hydroiodic acid bath for 24 h to maximize conductivity of rGO, followed by washing with saturated sodium bicarbonate aqueous solution, water, and methanol, respectively, and air dried.

Fabrication of rGO/PEDOT: PSS films

rGO/PEDOT: PSS film was solution cast on an untreated glass substrate. To parepare the rGO/PEDOT: PSS film in LLC phase, the concentrated 8:2 GO/PEDOT: PSS mixture with PEG-600 was poured onto a glass slide with 1 mm thick PDMS spacer, and blade coated to remove excess dispersion on top and to make sure the surface of the coating was flat and smooth. The glass slide with coated 8–2 GO/PEDOT: PSS film was placed in an oven at 60 °C overnight for drying. The dried film was peeled off by inserting a blade between the film and the glass substrate. The freestanding film was then immersed in hot (65 °C) hydroiodic acid for reduction, followed by washing with saturated sodium bicarbonate aqueous solution, water, and methanol, respectively, and air dried. The dried 8–2 rGO/PEDOT: PSS film was about 50 μm thick, which matched the diameter of the 8–2 rGO/PEDOT: PSS fiber actuator.

Fabrication of rGO/PEDOT: PSS film actuators w/o LC phase

The precursor GO/PEDOT: PSS dispersion was prepared by mixing 10 mg/mL aqueous GO dispersion with 1.1 wt% PEDOT: PSS water solution at a weight ratio of 8:2, followed by adding 10 wt% PEG-600, to a total volume of 4 mL. The mixture was then diluted 5 times to a total concentration of approximately 2 mg/mL, followed by 8 h vortex homogenization. The diluted precursor was poured onto a glass slide with 4 mm thick PDMS spacer. The glass slide with coated dispersion was placed in the 60 °C oven overnight. The dried film was peeled off from the glass substrate. The freestanding film was then immersed in hot (65 °C) hydroiodic acid for reduction, followed by washing with sodium bicarbonate, water, and methanol, respectively, and air dry. The dried 8–2 rGO/PEDOT: PSS film with no LC phase was about 50 μm in thickness, which matched the diameter of the rGO/PEDOT: PSS fiber actuator.

Characterizations

The polarized optical microscopy (POM) images were taken from an Olympus BX61 Motorized Microscope with crossed polarizers. The in situ digital images under crossed polarizers during the coagulation process were taken from a home-built optical setup equipped with polarizers using a Nikon D5600 DSLR Camera. The thermal IR images were taken by a FLIR C2 1.1 IR camera. The cross-sectional SEM images were obtained from FEI Quanta 600 Environmental Scanning Electron Microscopy (ESEM) at 10 kV electron beam under 0.50 Torr vacuum pressure. The thermogravimetric analysis (TGA) was carried out using a TA Instruments SDT Q600 TGA&DSC machine, from 0 °C to 800 °C with a heating speed of 10 °C/min in nitrogen environment. The resistance of the rGO/PEDOT: PSS fibers was measured by a Innova 3320 multimeter. The conductivity of the fibers was measured by a Jandel RM 3000 Multi Height Four-Point Probe and normalized by the thickness.

Small-Angle X-ray diffraction

The X-ray diffraction patterns were collected by a Xeuss 2.0 Dual Source Environmental X-ray Scattering System using copper source with 1.54 Å wavelength at 50 kV and 0.6 mA current. Two sets of slits used are 0.7*0.7 mm and 0.4*0.4 mm, respectively. The sample chamber was under vacuum environment at 20 °C, the sample-to-detector distance was 177 mm, which corresponding to a measurement 2θ value range of 0.92° to 43°. GO and GO/PEDOT: PSS fibers were exposed to X-ray for 1200 s, while rGO and rGO/PEDOT: PSS were measured using 3600 s exposure time due to the smaller diameters. All data analysis and transformation (azimuthal integration and azimuthal profile) were done in the Foxtrot analysis software.

Mechanical testing

Mechanical testing of GO/PEDOT: PSS fibers, rGO/PEDOT: PSS fibers and films were performed on an Instron 5564 Tabletop Universal Testing Machine. A tensile load cell with capability of 10 N was used. All the samples had the same initial length of 10 cm and were pulled at a speed of 5 mm/min till breakage. The stress–strain curves were calculated from the force–displacement curve, the diameter (cross-section for the films), and the initial gauge length of the fibers or films.

Actuation behaviors

The electrostatic actuation was performed by connecting one end of the fiber to the positive electrode of the high voltage power supply (Spellman UM 8–40 High Voltage Converter controlled by a Labview program) and fixing that end of the fiber onto an iron stand so the other end of the fiber was free to move. The ground of the power supply was connected to a conductive plate that was far away from the fiber. All the actuation tests were recorded as 120 fps videos by a Nikon D5600 DSLR Camera and processed by Tracker software for accurate bending angle and speed analysis.

Fiber plying

The plying machine (Ropewalk 'PLANETARY') was assembled with customize designed and 3D printed (Ultimaker 3 Extended) spool holders. For plying, 2–4 individual fibers, 8–2 rGO/PEDOT: PSS fiber and commercial nylon yarn were winded onto respective spools and loaded onto the plying machine. The angular speed of the rotating plate and the linear speed of the collecting spool were controlled to achieve the desired twist insertion to each yarn actuators fabricated. The twist insertion in the unit of twist per centimeter can be calculated by the following equation:

$$Twistinsertion = \frac{\omega_{spinning}}{v_{collectionspool}} = \frac{\omega_{spinning}(rpm)}{\omega_{collectionspool} * 2\pi r_{collectionspool}} \quad (2)$$

To preserve the straight shape without any pre-buckling, a twist insertion of 20 twist/cm was used for all the yarn actuators in this work. Notably, all the twists were inserted into the yarn,

not the individual fibers. All the fibers were hold in place at one end throughout the process to make sure the relative positions of the dense and sparse sides remained unchanged, so that the yarn actuator could still bend towards the sparse side as the individual fiber did. Moreover, all the yarns fabricated were able to sustain the inserted twist without any additional fixture due to the well-balanced friction between the individual fibers. However, to make sure the yarns do not untwist and change their response to high voltage during the repeated actuation cycles, additional fixtures were added to all yarn actuators at both ends after twist insertion using scotch tape.

Work capacity and power density measurement

The work capacity (J/kg) was calculated based on the weightlifting experiments. Weights with different known masses were hanged below the rGO/PEDOT: PSS fiber or yarn actuator that was connected to the high voltage power supply. The actuation response was recorded as 120 fps videos and analyzed using the Tracker software for accurate bending angle and response time measurement. The work capacity was calculated by the following equation:

$$WorkCapacity = \frac{m_{obj} g l \cdot (1 - cos\alpha)}{m_a} \quad (3)$$

where m_{obj} is the mass of the weight being lifted, g is the gravitational acceleration, l is the length of the actuator, α is the bending angle, and m_a is the mass of the actuator itself. The power density (W/kg) could then be calculated by dividing the work capacity over the response time, as shown below:

$$PowerDensity = WorkCapacity/ResponseTime \quad (4)$$

The results reported in the paper were averaged over 5 different fiber/yarn actuators fabricated with the same method.

Generated Stress, strain and efficiency calculation

Due to the signal interference from the high voltage power supply on the electronic powered force sensor, the stress and efficiency of the actuator were recalibrated. The stress was calculated by the mass of the load in the weightlifting experiment and the cross-section area of the fiber or yarn actuators. The cross-section area of the yarn actuator was estimated by measuring the diameter of the yarn and assume it had a circular shape. This indirect way of calculating the stress could be inaccurate as the force was not exerted exactly along the length direction of the actuator during the bending actuation. The actual stress generated was larger than the calculated values. Given θ was generally small in the weightlifting experiment, the difference could be ignored.

The actuation strain mentioned in this work were all linear strains in the vertical direction, which was calculated by the vertical displacement and the original actuator length: $l(1 - cos\alpha)/l = 1 - cos\alpha$.

The efficiency of the actuation was calculated by dividing the output power over the input power, the detailed equation is

$$Efficiency = \frac{m_{obj} g l \cdot (1 - cos\alpha)/ResponseTime}{V_{input} \times I_{input}} \quad (5)$$

where V_{input} and I_{input} are the input voltage and current, respectively. The numerator is the calculated the output power in the weightlifting experiment

Demonstration of robotic integration

For the flapping wing demonstration, the wing skeleton with holes for yarn threading was cut from a PET sheet by a Cricut Explore Air 2 machine. Four r-n-r yarn actuators were first threaded through the small holes on the PET skeleton and fixed by Scotch tape, then through the large hole on the bottom (**Fig. S21**). The four yarns were connected to the power supply for actuation test. For the fish tail demonstration, the skeleton with holes was also cut from a PET sheet using the Cricut Explore Air 2 machine. 8 r-n-r yarn actuators were threaded through the small holes on the skeleton and fixed by Scotch tape, then through the large hole on the bottom (Fig. S21). The yarns and the skeleton were sealed by Kapton tape for insulation on both sides. The above steps were repeated for the other piece of the fish tail structure. The two pieces of fish tail including the 16 yarn actuators were connected to the power supply for actuation test. The actuation tests were conducted using an Artimus Robotics portable high voltage power supply and control software, the input voltage was 5 kV square wave with a frequency of 5 Hz–10 Hz.

The actuation behaviors were recorded as 120 fps videos (Video S3-S4) and processed by Tracker software for measuring the actuation angle and time.

Author contributions

Y.G. and S.Y. conceived the research ideas; Y.G. and J.L. prepared and fabricated the materials; Y.G. conducted X-ray, mechanical, and electrical characterizations; Y.G. conducted the characterization and analytical analysis, Y.G. and J.L. designed and performed the robotics demonstrations; Y.G., J.L. and S.Y. wrote the manuscript; and S.Y. supervised the research.

Data availability statement

All data needed to draw the conclusions of the paper are present in the paper and/or the Supplementary Materials. Additional datasets that support the findings of this study are available from the corresponding authors upon reasonable request.

CRediT authorship contribution statement

Yuchong Gao: conceived research ideas, prepared and fabricated materials, conducted characterization and analysis, designed and prepared the robotics demonstrations, co-wrote the manuscript. **Jiaqi Liu:** prepared and fabricated materials, designed and prepared the robotics demonstrations, co-wrote the manuscript. **Shu Yang:** conceived research ideas, solicited funding, supervised research and co-wrote the manuscript.

Data availability

Data will be made available on request.

Declaration of Competing Interest

The authors declare that they have no known competing financial interests or personal relationships that could have appeared to influence the work reported in this paper.

Acknowledgements

We acknowledge the support by Army Research Office (ARO) through the MURI program, #W911-NF-1810327 . We acknowledge use of SEM instruments and the Dual Source and Environmental X-ray Scattering facility supported by the National Science Foundation Materials Research Science and Engineering Center (DMR-1720530) at the University of Pennsylvania. The purchase of the Dual Source and Environmental X-ray Scattering facility was made possible by a National ScienceFoundation Major Research Instrumentation (MRI) grant (17-25969), an Army Research Office (ARO) Defense University Research Instrumentation Program (DURIP) grant (W911NF-17-1-0282) and the University of Pennsylvania. We gratefully acknowledge Dr. Lishuai Jin and Dr. Baohong Chen for discussion on the analytical analysis.

Appendix A. Supplementary material

Supplementary data to this article can be found online at https://doi.org/10.1016/j.mattod.2023.08.003.

References

[1] P. Brochu, Q. Pei, Macromol. Rapid Commun. 31 (2010) 10–36.
[2] D.R. Higueras-Ruiz et al., Bioinspir. Biomim. 17 (2021) 011001.
[3] S.M. Mirvakili, I.W. Hunter, Adv. Mater. 30 (2018) 1704407.
[4] J. Zhang et al., IEEE Trans. Rob. 35 (2019) 761–781.
[5] T. Guin et al., Nat. Commun. 9 (2018) 2531.
[6] S.M. Mirvakili, D. Sim, I.W. Hunter, R. Langer, Sci. Robot. 5 (2020) eaaz4239.
[7] J. Liu et al., Adv. Intell. Syst. 2 (2020) 1900163.
[8] H. Cheng et al., Adv. Mater. 26 (2014) 2909–2913.
[9] J. Mu et al., Science 365 (2019) 150–155.
[10] Q. He et al., Sci. Adv. 5 (n.d.) eaax5746.
[11] Q. He et al., Sci. Rob. 6 (2021) eabi9704.
[12] R.J. Wood, E. Steltz, R.S. Fearing, Sens. Actuators Phys. 119 (2005) 476–488.
[13] J. Foroughi et al., Science 334 (2011) 494–497.
[14] J. Li et al., Nano Lett. 11 (2011) 4636–4641.
[15] V. Palmre et al., Sci. Rep. 4 (2014) 6176.
[16] R. Pelrine et al., Science 287 (2000) 836–839.
[17] M. Duduta et al., Proc. Natl. Acad. Sci. 116 (2019) 2476–2481.
[18] Y. Shi et al., Science 377 (2022) 228–232.
[19] A.E. Aliev et al., Science 323 (2009) 1575–1578.
[20] X. Yu et al., Nat. Rev. Mater. 2 (2017) 1–13.
[21] Z. Xu, C. Gao, ACS Nano 5 (2011) 2908–2915.
[22] R. Narayan et al., Adv. Mater. 28 (2016) 3045–3068.
[23] Z. Xu, C. Gao, Mater. Today 18 (2015) 480–492.
[24] W.K. Chee et al., J. Phys. Chem. C 120 (2016) 4153–4172.
[25] Z. Yin et al., Adv. Energy Mater. 4 (2014) 1300574.
[26] Y. Wang et al., Sci. Adv. 3 (2017) e1602076.
[27] F.-P. Du et al., Sci. Rep. 8 (2018) 6441.
[28] D.R. Dreyer et al., Chem. Soc. Rev. 39 (2010) 228–240.
[29] J. Zhang et al., Sci. 6 (2020) 254–265.
[30] Q. Wei et al., Adv. Mater. 25 (2013) 2831–2836.
[31] B. Fang et al., Adv. Mater. 32 (2020) 1902664.
[32] C. O'Mahony et al., Micromachines 10 (2019) 99.
[33] W. Eom et al., Nat. Commun. 12 (2021) 1–8.
[34] A. Chortos et al., Adv. Funct. Mater. 31 (2021) 2010643.
[35] J. Zhu et al., J. Appl. Phys. 108 (2010) 074113.
[36] C.S. Haines et al., Science 343 (2014) 868–872.
[37] M.D. Lima et al., Science 338 (2012) 928–932.
[38] H. Yuk et al., Nat. Commun. 8 (2017) 14230.
[39] S. Liu et al., Adv. Funct. Mater. 20 (2010) 3266–3271.
[40] Q. Liu et al., Sci. Rob. 6 (2021) eabe6663.
[41] J. Sun et al., Small 17 (2021) 2103700.
[42] P. Li et al., Adv. Funct. Mater. 30 (2020) 2006584.
[43] Z. Xu et al., Adv. Mater. 28 (2016) 6449–6456.